3D time-domain spectral inversion of resistivity and full-decay induced polarization data – full solution of Poisson's equation and modelling of the current waveform

Line Meldgaard Madsen[1], Gianluca Fiandaca[1,2], Esben Auken[1]

[1] HydroGeophysics Group, Department of Geoscience, Aarhus University,
C. F. Møllers Alle 4, 8000 Aarhus C, Denmark.
[2] Dipartimento di Scienze della Terra "A. Desio", Università degli Studi di Milano,
Via Cicognara 7, 20129 Milano, Italy

Corresponding author:
Line Meldgaard Madsen, linemeldgaard@geo.au.dk, +45 27851816

Short title:
3D spectral inversion of TD IP

Submitted: 07.12.2019
Resubmitted: 11.05.2020
2nd resubmission: 07.09.2020

Note: The inversion algorithm presented in this paper is available at https://hgg.au.dk/software/aarhusinv/ and is free to use for non-commercial purposes. Data, input files, and data processing scripts can be accessed upon request to the corresponding author.

Abstract

We present a new algorithm for 3D forward modelling and spectral inversion of resistivity and time-domain full-decay induced polarization (IP) data. To our knowledge, all algorithms available for handling 3D spectral inversion of full-decay IP data use a time-domain approximation to Poisson's equation in the forward response. To avoid this approximation, we compute the response in the frequency domain solving the full version of Poisson's equation for a range of frequencies (10^{-8}-10^{4} Hz) and then transform the response into the time domain, where we account for the transmitted current waveform. Solving Poisson's equation in 3D is computationally expensive and in order to balance accuracy, time, and memory usage we introduce the following: 1) We use two separate meshes for the forward response and the model update, respectively. The forward mesh is an unstructured tetrahedral mesh allowing for local refinements whereas the model (inversion) mesh is a node-based structured mesh, where roughness constraints are easily implemented. By decoupling the two meshes, they can be tuned for optimizing the forward accuracy and the inversion resolution, independently. 2) A singularity removal method known from resistivity modelling has been adapted to the complex IP case and is applied to minimize the numerical errors caused by the fast changing potential close to the source electrodes. The method includes splitting the potential field into a primary part (response of a homogenous background) and a secondary part (from the anomalies). Two different forward meshes are then used to compute the forward response: a dense mesh for the primary potential field (only computed once for each frequency) and a coarser mesh for the secondary potential field (computed in each iteration step of the inversion). With this method, the singularity is minimized and the memory usages is decreased significantly at the same time. 3) Finally, we are sparsing (down-sampling) the Jacobian matrix based on a threshold value of the normalized sensitivity. The Jacobian computation is performed by time-transforming the

frequency-domain Jacobian obtained through the adjoint method. The Jacobian down-sampling is carried out before the time-transform in the frequency domain, thus avoiding the time-transformation of the Jacobian elements with negligible sensitivity. We invert resistivity data and all IP time-gates simultaneously and use the Gauss-Newton model update to minimize the L2 misfit function. We invert the resistivity data and all IP time-gates simultaneously and use the Gauss-Newton model update to minimize the L2 misfit function. We demonstrate the performance of our inversion approach with a synthetic data example with 3D anomalies and a field example, where lithology logs verify the results. The datasets contain 1256 quadrupole measurements with 33 IP time-gates each. The inversions results show good data fits and model retrieval. The inversion takes approximately one hour per iteration using four CPUs. With this speed and accuracy, we believe this modelling and inversion approach will be a strong tool for 3D spectral inversion of resistivity and full-decay IP field data for both surface and borehole applications.

Key words:

Electrical properties, Hydrogeophysics, Electrical resistivity tomography (ERT),

Inverse theory, Numerical modelling

1. Introduction

The direct current (DC) resistivity and induced polarization (IP) geophysical methods are widely applied for near-surface investigations. In recent years, research has focused on the spectral content of the IP signal (Kemna *et al.*, 2012), which can be linked to the geological and hydrological properties of the subsurface through petro-physical relations (e.g. Revil and Florsch, 2010, Weller *et al.*, 2015). Accordingly, time-domain spectral IP is increasingly applied in environmental surveys, e.g. for mapping of contamination and old landfills (e.g. Gazoty *et al.*, 2012, Wemegah *et al.*, 2014, Johansson *et al.*, 2015), for field-scale estimations of hydraulic conductivity (e.g. Attwa and Günther, 2013, Maurya *et al.*, 2018), and for monitoring of contaminant remediation projects (e.g. Flores Orozco *et al.*, 2015, Flores Orozco *et al.*, 2019, Nivorlis *et al.*, 2019). These applications require a robust and accurate spectral inversion scheme, which is able to handle large datasets from 3D surveys with thousands of quadrupole measurements within a reasonable computation time and with reasonable memory usage. However, to our knowledge, no algorithms exist for 3D time-domain spectral inversion of full-decay IP data (i.e. disregarding integral-chargeability and one-frequency approaches), which fulfil these requirements. In this paper, we therefore present an algorithm for 3D time-domain spectral inversion of resistivity and full-decay IP data with a focus on balancing accuracy, speed, and memory usage when inverting large-scale datasets.

In the frequency domain, the IP effect of the subsurface can be described by the 3D-distributed, frequency-dependent, complex conductivity, σ^*, which is intended as an effective conductivity that contains both conduction and polarization effects of free and bound charges, as $\sigma^* = \sigma^*_{free} + i\omega\varepsilon^*_{bound}$, where $i = \sqrt{-1}$ is the imaginary unit, ω is the angular frequency and $\varepsilon^*_{bound} = \varepsilon_0(1 + \chi_e)$ is the electric permittivity, defined in terms of the free-space permittivity ε_0 and the electric susceptibility χ_e. By neglecting

electromagnetic (EM) effects, the complex potential, $u^*(\omega) = u'(\omega) + iu''(\omega)$, measured in an IP investigation, is linked to the complex conductivity through Poisson's equation:

$$\nabla \cdot \boldsymbol{j}_s^*(\omega, \boldsymbol{r}) = \nabla \cdot \left(\sigma^*(\omega, \boldsymbol{r}) \boldsymbol{E}^*(\omega, \boldsymbol{r})\right), \quad (1)$$

where $\boldsymbol{j}_s^*$ is the applied source current density, $\boldsymbol{r} = (x, y, z)$ is the spatial location, and $\boldsymbol{E}^*(\omega, \boldsymbol{r}) = -\nabla u^*(\omega, \boldsymbol{r})$ is the complex electric field.

The IP forward responses are modelled by computing the complex potential (equation 1) for a range of frequencies. In a frequency-domain spectral inversion, the complex conductivity distribution is retrieved independently, frequency by frequency, or simultaneously for all frequencies, which makes it possible to define smoothness constraints between the conductivity values of adjacent frequencies (e.g. Günther and Martin, 2016). The spectral content can then be presented, for instance, by fitting Cole-Cole models (Cole and Cole, 1941, Pelton *et al.*, 1978) to the resulting complex potentials in each model cell (e.g. Loke *et al.*, 2006). As an alternative, it is possible to invert directly for the Cole-Cole parameters (e.g. Blaschek *et al.*, 2006) and thereby decrease the length of the model vector during the model update (i.e. from the number of frequencies to the number of model parameters).

In the time domain, Poisson's equation is given as a convolution between the conductivity and the electric field as a function of the time t (e.g. Kemna 2000):

$$\nabla \cdot \boldsymbol{j}_s(t, \boldsymbol{r}) = \nabla \cdot \left(\int_0^\infty \sigma(t', \boldsymbol{r}) \boldsymbol{E}(t - t', \boldsymbol{r}) dt'\right), \quad (2)$$

where $\sigma(t)$ is the inverse Laplace transform of $\sigma^*(\omega)$ and $\boldsymbol{E}(t, \boldsymbol{r}) = -\nabla u(t, \boldsymbol{r})$. To avoid the computationally demanding convolution, simplifications are often applied when modelling the forward response in time domain. The approach introduced by Seigel

(1959) is a famous simplification, which postulates that the applied source current density creates a distribution of current dipoles antiparallel to the electric field with a current volume moment corresponding to the current density $\boldsymbol{j}_P(\boldsymbol{r}) = \frac{\partial \boldsymbol{P}(\boldsymbol{r})}{\partial t} = -m(\boldsymbol{r}) \cdot \boldsymbol{j}_{free}(\boldsymbol{r})$, where $(\boldsymbol{P})$ is the polarization, m is the model-space chargeability and $\boldsymbol{j}_{free}$ is the primary current density. With this assumption, the total current density including polarization is given as $\boldsymbol{j} = \boldsymbol{j}_{free} + \boldsymbol{j}_P = \boldsymbol{j}_{free}(1-m) = \sigma_\infty(1-m)\boldsymbol{E}$, where σ_∞ is the conductivity when neglecting the polarization effects. The apparent chargeability (m_a), defined by Seigel (1959) as the potential measured just after current turn-off normalized by the DC (steady-state) potential, can then be modelled by solving the forward operator, $\nabla \cdot \boldsymbol{j}(\boldsymbol{r}) = \nabla\big(\sigma(\boldsymbol{r}) \cdot \boldsymbol{E}(\boldsymbol{r})\big)$, twice: once for σ_∞ and once for $\sigma_0 = \sigma_\infty\,(1-m)$ (Seigel, 1959, Oldenburg and Li, 1994). However, this approach implicitly neglects the convolution of equation (2), because the polarization $\boldsymbol{P}$ is not treated as the convolution of the electric field with the time-dependent electric susceptibility $\chi_e(t, \boldsymbol{r})$. Instead, the chargeability m is defined as a time-dependent property $m(t, \boldsymbol{r})$, which can be inverted for each time-gate.

More recently, studies have divided the IP decay into time-gates and used an explicit approximation to equation (2) to compute the forward response in each time-gate. Here, the convolution of equation (2) is replaced by a simple multiplication between the conductivity and the electric field (e.g. Yuval and Oldenburg, 1997, Hördt *et al.*, 2006, Hönig and Tezkan, 2007):

$$\nabla \cdot \boldsymbol{j}(t, \boldsymbol{r}) \cong \nabla \cdot \big(\sigma(t, \boldsymbol{r}) \cdot \boldsymbol{E}(t, \boldsymbol{r})\big)\,. \tag{3}$$

Hördt *et al.* (2006) and Hönig and Tezkan (2007) compared this approximate time-domain solution to the full frequency-domain solution and showed that the approximation is exact for homogenous half spaces and a good approximation for early

and late times of the decay curve in general. With the approach, an inversion is performed in each individual time-gate, and the spectral content of the IP signal is determined by combining the inversion results from the gates and fitting the resulting decay curves to a Cole-Cole model (e.g. Yuval and Oldenburg, 1997, Hördt *et al.*, 2006, Hönig and Tezkan, 2007). However, when inverting the time-gates independently, there is a risk of obtaining non-physical decays. This risk can be mitigated by inverting all time-gates at once as suggested by Yi *et al.* (2012) and Nivorlis *et al.* (2017). They also suggest adding constraints between the gates to avoid irregular shapes of the IP decays. However, it is questionable whether the constraints will prevent fitting "non-standard" IP decays (e.g. decays with changing signs) as described by Fiandaca *et al.* (2019). Despite simultaneous inversion of all time-gates, these time-domain approaches do not obey the physics of Poisson's equation as the approximation in equation (3) is still used.

Fiandaca *et al.* (2012, 2013) presented an approach for 1D and 2D spectral inversion of time-domain IP data, where the forward response is computed in the frequency domain, solving the full version of Poisson's equation, and then transformed into the time domain. In this way, the time-domain approximation (equation 3) is avoided. However, when using the resistivity and IP method to map subsurface geological structures with complex geometries, 1D and 2D inversion schemes are not always sufficient. For instance, in environmental surveys aiming to map contaminant plumes or injected remediation products (often using cross-borehole measurements), the anomalies are inherently 3D and often show high conductivity contrasts. In such cases, 3D modelling and inversion of the data are required. Algorithms do exist for handling 3D inversion of time-domain IP data (e.g. Karaoulis et al., 2013, Li & Oldenburg, 2000, Günther et al. 2017), however, these all apply an integral-chargeability approach or the approach presented by Seigel (1959) and Oldenburg & Li (1994) as outlined above.

In this paper, we present a 3D spectral inversion algorithm for resistivity and full-decay IP data. The inversion follows the approach of Fiandaca *et al.* (2012, 2013) and models the forward response in the frequency domain and then transforms it to the time domain, where the transmitted current waveform is taken into account. Solving Poisson's equation in 3D for many frequencies, which is required by IP modelling, is computationally expensive. We therefore present an adapted version of a singularity removal method (Coggon, 1971, Lowry *et al.*, 1989) and a triple-mesh approach (Günther *et al.*, 2006), previously applied for resistivity modelling. These methods have been adapted to the complex IP case and combined with a node-based definition of the model mesh. This is done in order to balance the modelling accuracy and the computational speed and memory usage. Furthermore, an efficient procedure for sparsing (down-sampling) the Jacobian is applied. The 3D modelling and inversion algorithm is validated on synthetic data and a field example.

2. Data and model space

In the following, the data vector ($\boldsymbol{d}$) is given by the DC potential (u_{DC}) and the IP potential (u_{IP}) in each time-gate of the IP decay. For the $i'th$ quadrupole measurement we have

$$\boldsymbol{d_i} = \left(u_{DC}, u_{IP,1}, \dots, u_{IP,N_{gates}}\right)^T, \tag{4}$$

where the DC potential is measured just before the current is changed and is defined by

$$u_{DC} = \frac{\int_{t_s}^{t_e} u(t')dt}{t_e - t_s}, \tag{5}$$

where t_s and t_e are the lower and upper limits of integration of the measured potential $u(t)$. The IP potential of the $j'th$ time-gate is defined by

$$u_{IP,j} = \frac{\int_{t_j}^{t_{j+1}} u(t')dt}{t_{j+1}-t_j}, \tag{6}$$

where t_j and t_{j+1} are the opening and closing times of the $j'th$ time-gate. Alternatively, the data vector can be defined by the apparent resistivity (ρ_a) and the apparent chargeability ($m_{a,j}$) in each time-gate, so

$$\boldsymbol{d_i} = (\rho_a, m_{a,1}, \dots, m_{a,N_{gates}})^T. \tag{7}$$

Here, the apparent resistivity (Ωm) is given by $\rho_a = K \cdot u_{DC}/I$, where K is the geometric factor and I is the injected current, and the apparent chargeability (mV/V) is given by $m_{a,j} = u_{IP,j}/u_{DC} \cdot 1000$.

In the model space, different parameterizations of the complex conductivity can be used to describe the spectral content. Table 1 gives an overview of some of the parameterizations that have been implemented. For the inversion examples presented in this study, we invert directly for the Maximum Phase Angle (MPA) Cole-Cole model parameter (Fiandaca *et al.*, 2018). The MPA model is a re-parameterization of the classic Cole-Cole model (Cole and Cole, 1941, Pelton *et al.*, 1978). Compared to the classic Cole-Cole model, the re-parameterization uses the maximum of the phase shift instead of the intrinsic chargeability, which minimizes the correlation of the model parameters in the inversion (Madsen *et al.*, 2017, Fiandaca *et al.*, 2018). The model space is defined by:

$$\boldsymbol{m} = \left(\log_{10}(\rho_0), \log_{10}(\varphi_{max}), \log_{10}(\tau_\varphi), \log_{10}(C)\right)^T. \tag{8}$$

Table 1: Implemented parameterizations of IP		
Parameterization	**Model parameters**	**Reference**
Resistivity Cole-Cole model	$\boldsymbol{m} = \{\rho_o, m_0, \tau_\rho, C\}$ $\rho^* = \rho_0 \left[1 - m_0(1 - \frac{1}{1+(i\omega\tau_\rho)^C})\right]$	(Cole and Cole, 1941, Pelton *et al.*, 1978).
Drake model	$\boldsymbol{m} = \{\rho_o, \omega_l, \varphi\}$ $\rho^* = K(i\omega + \omega_l)^{-b}$ $\rho_o = K(\omega_l)^{-b}$ $\varphi = \frac{\pi}{2} b \; for \; \omega > \omega_l$	(Van Voorhis *et al.*, 1973, Johansson *et al.*, 2015)
Constant Phase Angle (CPA)	$\boldsymbol{m} = \{\rho_o, \varphi\}$ As the Drake model, but with $\omega_l = 10^{-6} \, rad/s$	(Van Voorhis *et al.*, 1973, Johansson *et al.*, 2015)
Maximum Phase Angle Cole-Cole	$\boldsymbol{m} = \{\rho_0, \varphi_{max}, \tau_\varphi, C\}$ $\tau_\varphi = \tau_\rho(1 - m_0)^{1/2C}$ $\varphi_{max} = \tan^{-1}(\frac{\rho''(1/\tau_\varphi)}{\rho'(1/\tau_\varphi)})$	(Fiandaca *et al.*, 2018)

3. Forward modelling

We model the 3D resistivity and IP forward responses in the frequency domain for a range of frequencies using the finite element method. The responses are then transformed into the time domain for each quadrupole measurement and the transmitted current waveform is applied. The steps of the forward modelling are described in the following.

3.1 Finite element formulation

The frequency-domain 3D resistivity and IP forward operator (neglecting EM effects) is defined by Poisson's equation:

$$\nabla \cdot \left(\sigma^*(\omega, \boldsymbol{r}) \nabla u^*(\omega, \boldsymbol{r})\right) = -I\delta(\boldsymbol{r} - \boldsymbol{r_s}), \tag{9}$$

where $\sigma^*(\omega, \boldsymbol{r})$ and $u^*(\omega, \boldsymbol{r})$ are the previously described complex conductivity and electric potential, respectively, I is the electric current injected as a point source at $\boldsymbol{r_s} = (x_s, y_s, z_s)$, and δ is Dirac's delta function, such that $I\delta(\boldsymbol{r} - \boldsymbol{r_s}) = \nabla \cdot \boldsymbol{j}_s(\omega, \boldsymbol{r})$. Boundary conditions are enforced after Dey and Morrison (1979):

$$\frac{du^*(\omega, \boldsymbol{r})}{d\boldsymbol{n}} + v(\boldsymbol{r}, \boldsymbol{n}) u^*(\omega, \boldsymbol{r}) = 0 \text{ on } \Gamma = \Gamma_S \cup \Gamma_\infty , \tag{10}$$

where $\boldsymbol{n}$ is the outward normal of the respective boundary (Γ). At the surface-air interface (Γ_S), natural boundary conditions prohibit current flow through the surface with $v(\boldsymbol{r}, \boldsymbol{n}) = 0$. At the outer domain boundaries (Γ_∞), mixed boundary conditions describe the asymptotic behaviour of the potential field with $v(\boldsymbol{r}, \boldsymbol{n}) = (\boldsymbol{n} \cdot \boldsymbol{r})/|\boldsymbol{r}|^2$ (Dey and Morrison, 1979). The finite element method converts the boundary value problem into a minimization of an integral functional. By subdividing the modelling domain into elements, the integral can be evaluated for each element and the problem is reduced to a system of linear equations for each frequency, $\boldsymbol{A}^* \boldsymbol{u}^* = \boldsymbol{b}$, where $\boldsymbol{A}^*$ is a complex and symmetric coefficient matrix of size N_n x N_n (N_n being the number of nodes). The vector $\boldsymbol{u}^*$ (size N_n) holds the complex potentials at the nodes and the vector $\boldsymbol{b}$ (size N_n) holds the source term. For a more general introduction to the finite element method, the reader is referred to Jin (2015).

3.2 Singularity removal

Using equation (9), a singularity arises close to the source due to the delta function on the right-hand side. This means that the numerical approximations of the potential field become poor close to the electrodes. Coggon (1971) and Lowry *et al.* (1989) suggested

that this singularity can be removed by splitting the potential field into a primary part (background) and a secondary part. In the following, u_p^* is the complex primary potential caused by a current source in a homogenous half-space of conductivity σ_p^*. The complex secondary potential (u_s^*) is then caused by the anomalous conductivity $\sigma_s^*(\omega, \boldsymbol{r}) = \sigma^*(\omega, \boldsymbol{r}) - \sigma_p^*$. The secondary potential problem can be written as (Lowry *et al.*, 1989)

$$\nabla \cdot (\sigma^*(\omega, \boldsymbol{r}) \nabla u_s^*(\omega, \boldsymbol{r})) = \nabla \cdot \left((\sigma_p^* - \sigma^*(\omega, \boldsymbol{r}) \right) \nabla u_p^*) \,, \tag{11}$$

$$\frac{du_s^*}{d\boldsymbol{n}} + v(\boldsymbol{r}, \boldsymbol{n}) u_s^* = \frac{du_p^*}{d\boldsymbol{n}} + v(\boldsymbol{r}, \boldsymbol{n}) u_p^* = 0 \text{ on } \Gamma, \tag{12}$$

where the current density of equation (9) is removed and the expression only depends on the primary field, which can be computed analytically for flat-Earth models. However, the singularity is only removed if the primary conductivity equals the local conductivity at the source (Zhao and Yedlin, 1996). In the inversion, we use the conductivity at the source (interpolated from the connected elements) from the previous model iteration as the primary conductivity, which in this way is updated for each source individually. To avoid computing the primary potential for each iteration, it is only computed once for each source for σ = 1 S/m and then scaled by the conductivity of the source node at the respective iteration, as suggested by Rücker *et al.* (2006). For each frequency, the forward problem (equation 11) is now reduced to a system of linear equations: $\boldsymbol{A}^{\sigma^*} \boldsymbol{u_s^*} = (\boldsymbol{A}^{\sigma_p^*} - \boldsymbol{A}^{\sigma^*}) \boldsymbol{u_p^*}$, where $\boldsymbol{A}^{\sigma_p^*}$ may be evaluated as $\boldsymbol{A}^{\sigma=1} \sigma_p^*$ to avoid computing the coefficient matrix for each source individually (see Rücker *et al.*, 2006).

In case of topography, the primary potential field must be computed numerically by evaluating equation (9). The accuracy of the response is then improved by refining the forward mesh close to the source electrodes. However, increasing the number of nodes in the forward mesh increases the computation time and memory usage, and we therefore

follow the approach of Günther *et al.* (2006), where two different forward meshes are applied: a locally refined mesh for computing the primary potential and a coarser mesh for the secondary potential (described further below). As the primary potential is computed only once (for $\sigma = 1\ S/m$) and only the secondary potential has to be updated in the inversion, this approach decreases the computation time and memory usage significantly.

3.3 Implementation

The algorithm is implemented using Fortran 90. The frequency-domain IP forward response is obtained by solving equation (11) for a range of frequencies, typically $10^{-8} < \omega < 10^{4}$ Hz with two to five frequencies per decade (see discussion in the next paragraph). In addition, the DC potential is computed as the response of frequency zero ($\omega = 0\ Hz$). For each source electrode, we calculate the potential field in the entire modelling domain, and the quadrupole responses are then computed by superposition of the potentials at the potential electrodes. This method is efficient as all electrodes are used more than once, and it allows the code to handle multiple current injections (i.e. current injected in more than two electrodes at the same time).

The coefficient matrix ($\boldsymbol{A}^{\sigma^*}$) of the linear system of equations generated from equation (11) holds the boundary conditions and thus depends on the location of the source electrode. As suggested by Rücker *et al.* (2006), $\boldsymbol{A}^{\sigma^*}$ is computed for an average source position, so it only has to be computed once. The linear system can then be solved in one go with multiple right-hand sides, so $\boldsymbol{A}^{*(N_n\ x\ N_n)}\boldsymbol{u}^{*(N_n\ x\ N_s)} = \boldsymbol{b}^{(N_n\ x\ N_s)}$ (N_n being the number of nodes and N_s being the number of sources). We store the sparse matrices in compressed sparse row (CSR) format to save memory and solve for the potentials

using the direct solver Intel MKL PARDISO (Schenk and Gärtner, 2018), which works with an OpenMP parallelization (e.g. Chapman *et al.*, 2007) and applies a lower-upper (LU) decomposition.

3.4 Time-transform

When the forward response has been computed for all frequencies and superposition has given us the quadrupole responses, these responses are transformed into the time-domain. The inverse Fourier transform of the frequency-domain step response, $u^*(\omega)/i\omega$, gives us the time-domain step-on response,

$$u_{step-on}(t) = \int_0^\infty Im\left(\frac{u^*(\omega)}{i\omega}\right) \omega \, \mathrm{J}_{1/2}(\omega t)\, d\omega, \tag{13}$$

where the Fourier transform is expressed by a Hankel transform of the imaginary part in terms of $J_{1/2}$, i.e. the Bessel function of order 1/2. In this way, the integral can be evaluated using the Fast Hankel transform as described by Johansen and Sørensen (1979).

To ensure the accuracy of the Hankel transform, 10 points per decade are required as input from the frequency-domain response. However, the frequency-domain kernels are much smoother than the transform coefficients. It is therefore possible only to calculate the frequency-domain response for a smaller number of points per decade (typically two to five) and then use cubic splines to interpolate the response to the 10 points per decade required by the fast Hankel transform (see Fiandaca *et al.*, 2013). Fiandaca *et al*. (2013) showed that computing the frequency-domain response for more than 5 points per decade does not increase the accuracy significantly. In the presented inversion code, the number of frequencies per decade used for the forward response can be tuned by the

user. The choice is then a trade-off between accuracy and computation time (computation time being directly proportional to the number of frequencies, as the parallelization is made within the single frequency).

3.5 Modelling the current waveform

The actual injected current waveform differs from an ideal instantaneous current step function, which means that the measured response also differs from a step response in equation (13). The duration of the injected current rarely exceeds the decay-time, which means that the measured pulse response has a smaller amplitude and a faster decay compared to a step response. Fiandaca *et al.* (2012) showed that with a current on-time of 4 s, the amplitude of the pulse response is 2/3 of the step response and that the signal decays to 50% three times faster. To avoid errors, we therefore model the pulse response following the procedure of Fiandaca *et al.* (2012). We first computed the step-off response from equation (13):

$$u_{step-off}(t) = u_{DC} - u_{step-on}(t)\,, \tag{14}$$

where $u_{DC} = u(\omega = 0)$. The pulse response (u_{pulse}) is then computed by superposition of two time-shifted step-off responses of opposite sign:

$$u_{pulse}(t) = \sum_{i=1}^{2}(-1)^i u_{step-off}(t + (i-1)T_{on}), \tag{15}$$

where T_{on} is the current on-time. Due to stacking, the injected current waveform is composed by a sequence of alternating pulses, where the decaying potential from the $j'th$ pulse will affect the potential response of all the following pulses. For a 50% duty cycle, this effect is modelled following Fiandaca *et al.* (2012), and the averaged potential after stacking is computed as

$$u_{stack}(t) = \frac{1}{N_{stack}} \sum_{j=1}^{Nstack} (-1)^{j+1} \sum_{k=1}^{j} \sum_{i=1}^{2} (-1)^{i+k} u_{step-off}\Big(t + (i-1)T_{on} + (j-k)\big(T_{on} + T_{off}\big)\Big). \quad (16)$$

Equation (16) holds for both the on-time and the off-time of the signal and should be used to compute the apparent chargeability as well as the apparent resistivity in equation (4) to equation (7).

4. Multi-mesh approach

To discretize the 3D problem, we have adapted and combined the triple-grid inversion approach presented by Günther et al. (2006) and the voxel inversion approach of Christensen et al (2017). In the triple-grid approach, a coarse tetrahedral mesh is used for the inversion (the model mesh) and two finer discretized tetrahedral meshes (one for the primary potential field and one for the secondary potential field) are used to compute the forward responses. With this method, it is possible to obtain a high accuracy of the forward response, while keeping the computational demands of the inversion down. In our adaption of the triple-grid approach, the model mesh is a node-based structured mesh, which is spatially decoupled from the forward meshes. In the voxel inversion approach of Christensen et al (2017), the model parameters are defined on the nodes of a structured mesh, and then linked to the forward mesh (1D forward meshes in Christensen et al., 2017) through an interpolation function. In this study, two tetrahedral unstructured forward meshes and the node-based structured model mesh are combined in a multi-mesh approach, as explained in detail in the following.

4.1 Model mesh

In the structured model mesh used in the inversion, the values of the model parameters are defined on the nodes. The nodes are uniformly spaced in the x- and y-direction and with log-increasing spacing in the z-direction to compensate for the decreasing resolution with depth. Topography is incorporated by shifting the nodes in the z-direction (Figure 1a). An advantage of the structured model mesh (compared to an unstructured/tetrahedral mesh) is that roughness constraints (vertically and laterally) are easily applied between the neighbouring nodes and that the final model is easy to interpret – especially in layered environments. Furthermore, defining the model parameters on the model mesh nodes, and linking them to the forward meshes through an interpolation function (as explained in the next paragraphs), allows us to completely decouple the model and the forward meshes, without increasing the size of the forward meshes.

4.2 Forward

In the tetrahedral meshes, which are used to compute the forward responses (one mesh for the primary potential field and one mesh for the secondary potential field), the complex potentials are defined on the nodes and the complex conductivities are defined in the center of each element (making it uniform within the element). With the tetrahedral mesh, it is possible to locally refine the mesh around the source electrodes and let the volume of the tetrahedral elements increase toward the outer boundaries. This ensures a good accuracy of the forward response close to the source, while keeping the computational demands down.

The unstructured tetrahedral meshes are (in contrast to the structured model mesh) complicated to build and are therefore constructed using external software. As a first step, we build a 2D surface mesh using the mesh generator Triangle (Shewchuk, 1996), where the positions of the electrodes are defined, and triangulation gives us the output surface nodes. In the second step, elevation is added to the surface nodes and the surface mesh (now also with z-coordinates) is given as input to the mesh generator TetGen (Si, 2015), which generates the 3D tetrahedral mesh. The output mesh from TetGen is used for the secondary field, i.e. the secondary potential mesh (Figure 1b). As a third step, which only is needed in case of topography (where the primary field must be computed numerically), the secondary potential mesh is refined around the electrode to generate the primary potential mesh (Figure 1d). This is done using the secondary potential mesh as input to TetGen, together with a maximum node distance defined as a function of the distance to the nearest electrode.

4.3 Interpolation

The link between the model mesh and the forward meshes is established through an interpolation function following Christensen *et al.* (2017). The values of the model parameters (defined in the model mesh nodes) are interpolated to the forward mesh elements using an interpolation function f (using nearest neighbor or inverse distance):

$$\boldsymbol{p} = f(\boldsymbol{P}) = \boldsymbol{F} \cdot \boldsymbol{P}, \tag{17}$$

where the vector $\boldsymbol{p}$ holds the values of the model parameters in the forward mesh elements, and $\boldsymbol{P}$ holds the values in the model mesh nodes. $\boldsymbol{F}$ is the matrix representation of the interpolation function and contains the interpolation weights, which only depend on the relative distances. In this way, the model mesh nodes are not required to be part

of the forward mesh and no strict geometrical link needs to exist between the model mesh and the forward mesh.

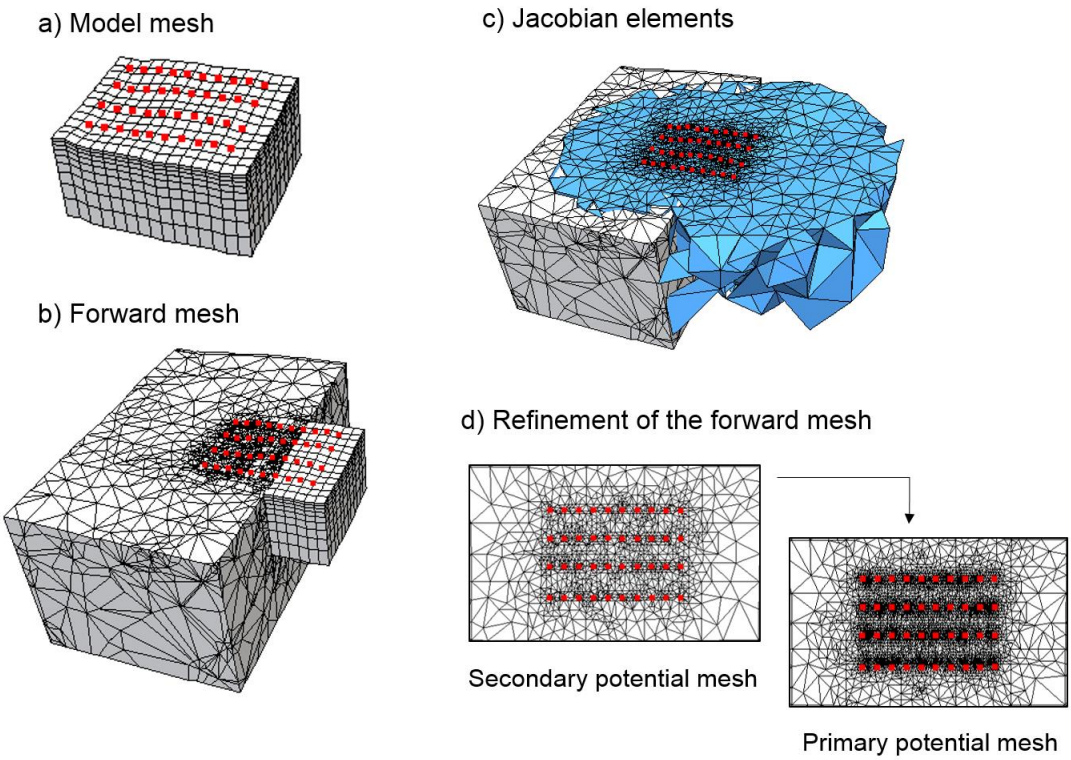

Figure 1: Illustration of the multi-mesh approach, where a node-based structured mesh is used for the model update in the inversion and a separate tetrahedral mesh is used for the forward calculations of the primary and secondary potential fields. The red dots show the location of the electrodes. a) The structured model mesh with the model parameters defined at the nodes. b) An inner section of the tetrahedral forward mesh, which is constructed around the model mesh nodes. c) The blue elements show the elements of the tetrahedral forward mesh that are used for computing the sensitivity. d) In case of topography, the primary potential field is computed numerically on a tetrahedral mesh, which is a refinement of the mesh nodes used for the secondary potential fields thus increasing the accuracy.

5. Sensitivity

The Jacobian matrix (or sensitivity matrix) is the partial derivative of the forward response ($\boldsymbol{d}$) with respect to the model parameters ($\boldsymbol{m}$):

$$\boldsymbol{G} = \frac{\partial \boldsymbol{d}}{\partial \boldsymbol{m}}. \tag{18}$$

As for the forward response, the Jacobian matrix is computed in the frequency domain and then transformed into the time domain. The complex frequency-domain Jacobian matrix ($\boldsymbol{G}^*_{FD}$) is computed for each frequency (ω) in each element (e) of the secondary potential mesh as:

$$G^*_{FD,i,k}(\omega, e) = \frac{\partial \boldsymbol{u}^*_i(\omega)}{\partial \boldsymbol{p}_k(e)} = \frac{\partial \boldsymbol{u}^*_i(\omega)}{\partial \boldsymbol{\sigma}^*(\omega,e)} \frac{\partial \boldsymbol{\sigma}^*(\omega,e)}{\partial \boldsymbol{p}_k(e)}, \tag{19}$$

where p_k is the $k'th$ model parameter ($k = 1,..4$) and u^*_i is the potential of the $i'th$ quadrupole measurement. The partial derivative of the conductivity with respect to the model parameter ($\partial\sigma^*/\partial p_k$) is computed by differentiation for each frequency separately, and the partial derivative of the potential with respect to the complex conductivity ($\partial u^*/\partial\sigma^*$) is then computed using the adjoint relationship (Spitzer, 1998):

$$\frac{\partial \boldsymbol{A}^*}{\partial \boldsymbol{\sigma}^*}\, \boldsymbol{u}^* = -\boldsymbol{A}^* \frac{\partial \boldsymbol{u}^*}{\partial \boldsymbol{\sigma}^*}. \tag{20}$$

The time-transform, the derivative defining the Jacobian, and the interpolation function (mapping the sensitivity from the forward mesh to the model mesh) are all linear operations, so we may write the time-domain Jacobian matrix as:

$$\boldsymbol{G}_{TD}(t) = L\big(\boldsymbol{G}^*_{FD}(\omega)\big) \cdot \boldsymbol{F}^T = L(\boldsymbol{G}^*_{FD}(\omega) \cdot \boldsymbol{F}^T), \tag{21}$$

where L is the time-transform (which also takes thecurrent waveform in account as described for the forward response) and $\boldsymbol{F^T}$ is the (transposed) matrix representation of the interpolation function of equation (17). By applying the transformation matrix before the time-transform, the number of time-transform operations is decreased (as the number

of nodes in the model mesh is significantly smaller than the number of cells in the forward mesh).

The number of elements in the frequency-domain Jacobian matrix is $N_d \cdot N_\omega \cdot N_e \cdot 4$ (where N_d is the number of data, N_ω is the number of frequencies, N_e is the number of mesh elements, and 4 is the number of model parameters). This number can easily exceed 10^9 elements and it is therefore useful to neglect elements of low sensitivities (e.g. small mesh elements far from the applied electrodes) in order to decrease the memory requirement. A way of sparsing (down-sampling) the Jacobian matrix, is by evaluating the absolute sensitivity of each mesh element against a threshold value as done, for instance, by Günther et al. (2006) for inversion of resistivity data. We have adapted this method to the spectral IP inversion case. In practice, we define an inner subdomain of the forward mesh (the secondary potential mesh) and compute the sensitivity with respect to the resistivity ($\omega = 0$ Hz) in all mesh elements of the inner subdomain, which extents five times the applied electrode spacing beyond the model mesh in all directions. In addition, we compute the sensitivity with respect to one middle range frequency (e.g. $\omega = 10^{-2}$ Hz for an applied frequency range of $10^{-8} < \omega < 10^{4}$ Hz). A mesh element will then be kept in the final Jacobian matrix, if either the resistivity or the representing IP sensitivity obeys

$$abs\left(\frac{du^*}{d\sigma^*(e)}\right)\frac{abs(\sigma^*(e))}{abs(u^*)}\frac{1}{volume(e)} \geq threshold. \tag{22}$$

For the remaining IP frequencies, the sensitivities are only computed for the kept mesh elements,decreasing computation time and memory usage significantly compared to threshold testing all elements and frequencies. Note that the forward response still needs to be computed using the full mesh, and only the matrix multiplication in equation (20) can be omitted for the nodes belonging to the disregarded mesh elements. The down-

sampling is carried out in the frequency domain, before the time-transform, in order to decrease both computation time and memory usage. For the inversion examples presented in this paper, the threshold value is 10^{-6} for both resistivity and IP data. This threshold ensures the same convergence and final misfit within a few percent compared to using the full Jacobian matrix. Experience has shown that a threshold value between 10^{-6} and 10^{-5} is satisfying in most cases. Figure 1 (c) shows an example of a forward mesh, where the mesh elements contributing to the final Jacobian are shown in blue.

6. Inversion

The inversion is performed iteratively following the established practice of linearized approximation (Menke, 1989) in combination with the Levenberg-Marquardt adaptive minimization scheme (Marquart, 1963), where an adaptive damping value (λ) is used to stabilise the inversion (described further below). The $n+1'th$ model vector is given by

$$\boldsymbol{m}_{(n+1)} = \boldsymbol{m}_{(n)} + \left[\boldsymbol{G'}^{T}_{(n)}\boldsymbol{C'}^{-1}\boldsymbol{G'}_{(n)} + \lambda_{(n)}\boldsymbol{I}\right]^{-1} \cdot \left[\boldsymbol{G'}^{T}_{(n)}\boldsymbol{C'}^{-1}\delta\boldsymbol{d'}_{(n)}\right], \tag{23}$$

where the Jacobian matrix ($\boldsymbol{G'_n}$), the data vector update ($\delta\boldsymbol{d'}_{(n)}$), and the covariance matrix ($\boldsymbol{C'}$) and are given by

$$\boldsymbol{G'}_{(n)} = \begin{bmatrix} \boldsymbol{G}_{(n)} \\ \boldsymbol{I} \\ \boldsymbol{R} \end{bmatrix}, \tag{24}$$

$$\boldsymbol{d'}_{(n)} = \begin{bmatrix} \delta\boldsymbol{d}_{(n)} \\ \delta\boldsymbol{m}_{(n)} \\ \delta\boldsymbol{r}_{(n)} \end{bmatrix} = \begin{bmatrix} \boldsymbol{d}_{(n)} - \boldsymbol{d}_{obs} \\ \boldsymbol{m}_{(n)} - \boldsymbol{m}_{prior} \\ -\boldsymbol{R}\boldsymbol{m}_{(n)} \end{bmatrix}, \tag{25}$$

$$\boldsymbol{C'} = \begin{bmatrix} \boldsymbol{C}_{obs} & 0 & 0 \\ 0 & \boldsymbol{C}_{prior} & 0 \\ 0 & 0 & \boldsymbol{C}_{R} \end{bmatrix}. \tag{26}$$

In equation (24), $\boldsymbol{G}'$ contains the Jacobian matrix of the forward mapping (equation 21) as well as the matrices imposing the constraints on the prior information ($\boldsymbol{I}$) and the roughness constrains ($\boldsymbol{R}$), which are described in detail by Auken *et al.* (2014). In equation (25), the data update vector ($\boldsymbol{d}'_{(n)}$) is given by the difference between the $n'th$ forward response ($\boldsymbol{d}_{(n)}$) and the observed data ($\boldsymbol{d}_{obs}$), the difference between the $n'th$ model vector ($\boldsymbol{m}_{(n)}$) and the prior values ($\boldsymbol{m}_{prior}$), and the rougthness if the $n'th$ mode vector ($-\boldsymbol{R}\boldsymbol{m}_{(n)}$). In equation (26), the covariance matrix is given by the covariance on the observed data ($\boldsymbol{C}_{obs}$), the covariance on the prior information ($\boldsymbol{C}_{prior}$), and the covariance on the roughness constraints ($\boldsymbol{C}_R$). For each node in the model mesh, lateral constraints are made to the four neighbouring nodes in the x- and y-direction, and vertical constraints are made to the two neighbouring nodes in the z-direction. For a detailed description of how these constraints are implemented through $\boldsymbol{R}$ and $\boldsymbol{C}_R$, the reader is referred to Auken *et al.* (2014).

The adaptive damping parameter $\lambda_{(n)}$ is used to stabilize the inversion of the $\boldsymbol{G}'^{T}_{(n)}\boldsymbol{C}'^{-1}\boldsymbol{G}'_{(n)}$ matrix in the model update (equation 23) and to controls the size of the model update. The damping is determined by the maximum of the diagonal of the $\boldsymbol{G}'^{T}_{(n)}\boldsymbol{C}'^{-1}\boldsymbol{G}'_{(n)}$ matrix reduced by an iteration-dependent scaling factor f_n (Marquart, 1963, Auken *et al.*, 2014):

$$\lambda_{(n)} = \max diag\left(\boldsymbol{G}'^{T}_{(n)}\boldsymbol{C}'^{-1}\boldsymbol{G}'_{(n)}\right) \cdot f_n. \tag{27}$$

In IP inversions, the magnitudes of the Jacobian elements differ significantly among the model parameters (e.g. τ_φ spans a relative large value range and is usually poorly resolved, meaning that it often has a very small sensitivity compared to the other model parameters). To avoid overdamping the weakly resolved parameter types, equation (27)

is evaluated block-wise for each parameter type individually, as suggested by Lin *et al.* (2019). During the inversion, the value of the scaling factor f_n is decreased with the iteration number, thus increasing the step size of the model update. This is done in order to avoid very large variations in the model update, when the inversion is far from the model that minimizes the objective function.

The objective function minimized by equation (23) is given as

$$Q = \left(\frac{\delta \mathbf{d}'^T \mathbf{C}'^{-1} \delta \mathbf{d}'}{N_d + N_m + N_c}\right)^{1/2}, \tag{28}$$

where N_d is the number of data, N_m is the number of model parameters, and N_c is the number of constraints. The iteration stops when the decrease of the objective function between consecutive iterations becomes smaller than 1%. The full workflow of the inversion scheme is presented step-wise in Table 2.

Table 2: Steps in the inversion scheme

1. Read input files (data, topography, constrains, etc.).
2. Generate the model mesh.
3. Generate the forward mesh (for the secondary potential).
4. Refining the forward mesh (for the primary potential).
5. Model the primary potential for $\sigma_p = 1$ (analytically or numerically) and interpolate to the secondary mesh nodes.
6. Compute the complex conductivity from the model parameters.
7. Model the secondary potential, scale the primary potential, and compute the total potential
8. Transform the total potential into time-domain.
9. Compute the sparse FD Jacobian matrix.
10. Transform the Jacobian matrix into time-domain.
11. Update the model.
12. Repeat 6-12, until the decrease of the objective function becomes smaller than 1%.

7. Accuracy

The accuracy of the 3D resistivity and full-decay IP forward response and Jacobian matrix is tested against a highly accurate 1D solution (Fiandaca *et al.*, 2012), which also takes the current waveform into account. Using the MPA Cole-Cole parameterization (Fiandaca *et al.*, 2018), a synthetic three-layer model is defined by the model parameters: $\rho_0 = (100,500,100)$ Ωm, $\varphi_{max} = (4,20,4)$ mrad, $\tau_\varphi = (1,0.1,1)$ s, $C = (0.6,0.6,0.6)$, and $\text{thickness} = (7,7,-)$ m. We compute the 1D and 3D forward responses of the model for 20 quadrupoles (simulating a Schlumberger sounding) with |AB|/2 ranging from 3.75 m to 248.75 m and |MN|/2 from 1.25 m to 33.75 m limiting the geometrical factor to 3000 m. The current waveform has a 4 s on-time and a 4 s off-time. The IP decay is divided into 33 time-gates with log-distributed gate length and with fist center-gate-time at 2.3 ms. We compute the forward response using 26 frequencies ($10^{-8} - 10^{4}$ Hz) including the DC frequency (0 Hz).

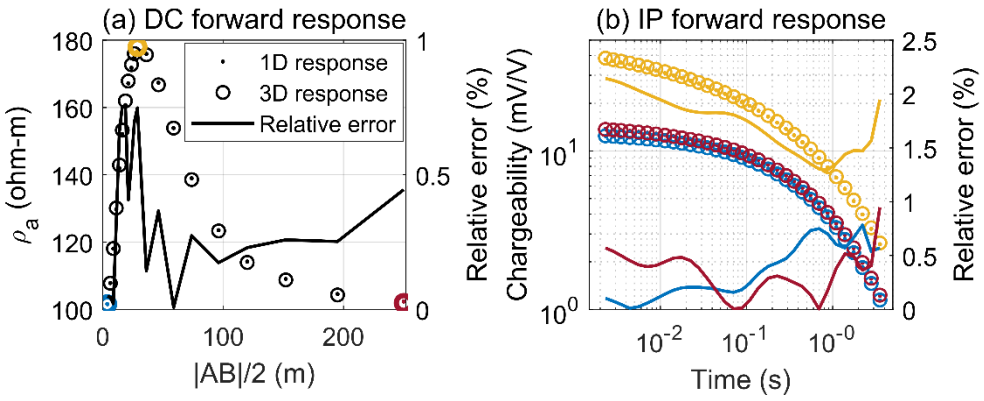

Figure 2: Accuracy of the 3D forward response shown as a comparison between the 3D and an accurate 1D computation (Fiandaca et al., 2012). (a) The DC resistivity value for 20 quadrupole measurements and their relative error to the 1D solution. (b) The accuracy of the modelled IP decays for three of the quadrupoles and their relative error to the 1D solution. The IP decays are color-coded to (a).

Figure 2 (a) shows the 1D and 3D DC resistivity forward responses together with the relative errors, which are below 1% for all 20 quadrupoles. Figure 2 (b) shows the IP decay for three of the quadrupoles (representing the three layers). The relative error is below 2.5% for all time-gates. The lower accuracy of the IP response compared to the DC responses depends on the splining of the frequency-domain kernels, as well as on propagation of the frequency-domain inaccuracy in the time-transform.

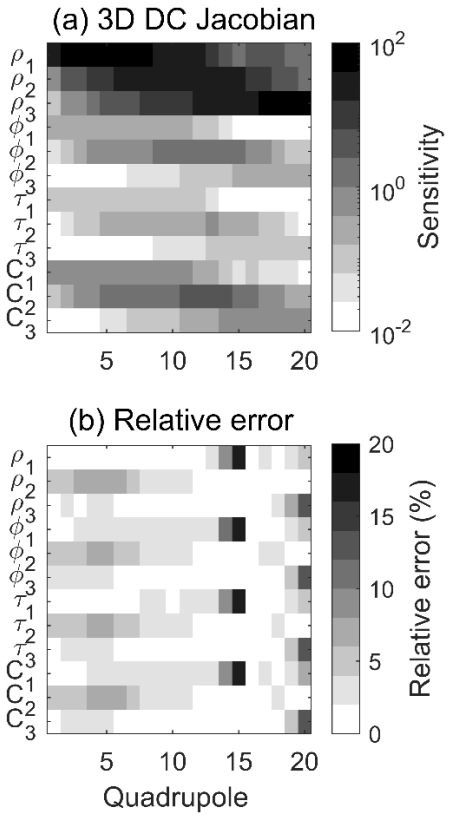

Figure 3: Accuracy of the 3D Jacobian shown as a comparison between the 3D computation and an accurate 1D algorithm (Fiandaca et al., 2012). (a) The 3D sensitivity shown for the DC resistivity values with respect to the model parameters ($\rho_0, \varphi_{max}, \tau_\varphi, C$) for each layer in a three-layer model. (b) The relative error of the DC Jacobian.

Figure 3 (a) shows the sensitivity of the 20 resistivity data with respect to the model parameters, and Figure 3 (b) shows the accuracy. The error is between 0 and 16% with a mean of 2.8% and a median of 2.0%. The high relative error at quadrupole 15 is associated with low sensitivity values. The 3D Jacobian matrix for the IP values follows the same trend. The mean error of the IP Jacobian matrix is 7.0%, while the median is 2.2%. Again, the high mean can be explained by a few elements with very low sensitivities, where the relative error raises above 100%.

8. Examples

In the following, we present a synthetic example and a field example of 3D inversion of resistivity and time-domain IP data. The field data were collected across a small stream in Grindsted, Denmark, where contamination from a nearby pharmaceutical factory is leaking into the stream (see Balbarini *et al.*, 2018). The field setup comprises four 80 m acquisition profiles with 10 m spacing between each profile. Each profile has 42 electrodes with a two meter spacing. The setup is shown in Figure 4 together with two boreholes, where we have lithological information. The boreholes, B1 and B2, are registered in the Danish national borehole database with identification number DGU 114.2570 and DGU 114.2507. The data were collected using a Terrameter LS instrument (ABEM) with a 4 s on-time and a 4 s off-time, sampling with a rate of 3750 Hz. A total of 1456 quadrupoles were measured using gradient array (Dahlin and Zhou, 2006). The IP decays are gated into 33 logarithmically spaced IP time-gates with first center-gate-time at 2.3 ms. Previous 2D inversion results of the data can be found in Maurya *et al.* (2018).

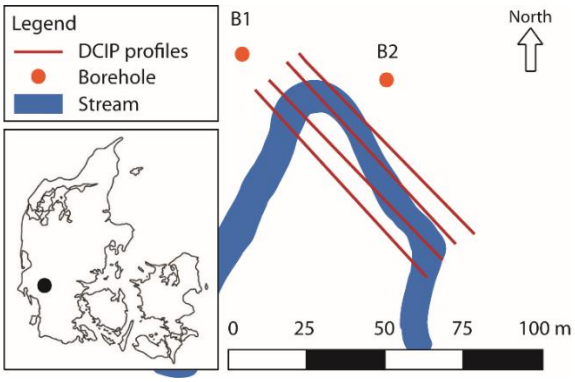

Figure 4: Sketch of the field setup across Grindsted Stream, Grindsted, Denmark. Four DCIP profiles of 80 m with 42 electrodes in each are laid out along the stream. Two boreholes with lithology logs, B1 and B2, are located close to the profiles.

Before we present the inversion of the field data, an inversion of synthetic data using the same electrode configurations is presented to verify the resolution capability.

8.1 Synthetic example

A synthetic model is constructed simulating a background formation with four box-formed anomalies defined by the MPA Cole-Cole parameters (equation 8). The synthetic model is shown in Figure 5 (a). The model mesh is constructed with 6210 nodes (46 x 9 x 15) with a 2 m spacing in the x-direction (along the profile) and 3.5 m in the y-direction. The node spacing in the z-direction increases logarithmically with depth with a minimum thickness of 0.5 m and a maximum depth of 25 m.

We compute the primary potential numerically in the forward modelling as must be done for the field example where topography is present. A standard deviation of 1% is assigned to the resistivity data and 10% to the IP data, which determine the balance between the resistivity and the IP data in the model update through the covariance matrix ($\boldsymbol{C_{obs}}$) in equation (24). Random noise with these standard deviations is added to the synthetic data to resemble the noise level in the field. For the roughness constraints ($\boldsymbol{C_R}$) imposed on the model update (equation 24 and 26), a factor of 1.5 (2.5 for τ_φ) is assigned for vertical constraints and 1.2 (1.6 for τ_φ) for lateral constraints between the model parameters of the neighboring mesh nodes. These are standard values (determined from experience with 1D/2D inversions), which ensure model smoothness without preventing the data fit. The constraint values for the time-constant (τ_φ) are larger, both because τ_φ is expected to span several decades in range and because it is less resolved (so weaker constraints are used to avoid over-smoothing the variations). The inversion is started from a homogenous half space model with the parameter values of the background

formation and converges after six iterations. The final data χ-misfit is 0.97 for the resistivity data and 1.06 for the IP data (the total χ-misfit, including constraints, is 0.71), where a data χ-misfit of one means that on average the model describes the data within the error bars. The inversion results are shown in Figure 5 (b) and show that all four anomalies are resolved. In general, the inversion overshoots the anomalies in their centers and undershoots at the edges, as a consequence of the L2 roughness constraints. The computation time and memory usage of the inversion are summarized in Table 3.

Table 3: Computation time and memory usage of 3D resistivity and IP inversions of synthetic data and field data using 4 CPUs. (Note: Topography is only added to the meshes in the field example, which explains the relative high number of nodes in the forward mesh used for the field example. The topography in the model mesh is added by vertically distorting the mesh nodes and the number of model mesh nodes is therefore the same for the two examples).

	Synthetic example	**Field example**
Model mesh	6210 nodes	6210 nodes
Forward mesh, secondary potential	11,340 nodes 62,428 elements	55,386 nodes 159,320 elements
Forward mesh, primary potential	76,419 nodes 394,447 elements	251,101 nodes 1,273,114 elements
Number of data	1456 quadrupoles 49,504 data (DC+IP)	1427 quadrupoles 31,697 data (DC+IP)
Inversion parameters	$\{\rho_0, \varphi_{max}, \tau_\varphi, C\}$	$\{\rho_0, \varphi_{max}, \tau_\varphi, C\}$
Forward response primary field	9 seconds	27 seconds
Frequency-domain forward response (26 frequencies)	30 seconds	150 seconds
Time transform of forward response	0.2 seconds	0.2 seconds
Frequency-domain Jacobian (26 frequencies)	22 minutes	47 minutes
Time transform Jacobian	6 seconds	10 seconds

Time per iteration	1.1 hours	1.3 hours
Total inversion time	10 hours (9 iterations)	18 hours (14 iterations)
Maximum memory	19,000 MB	37,000 MB

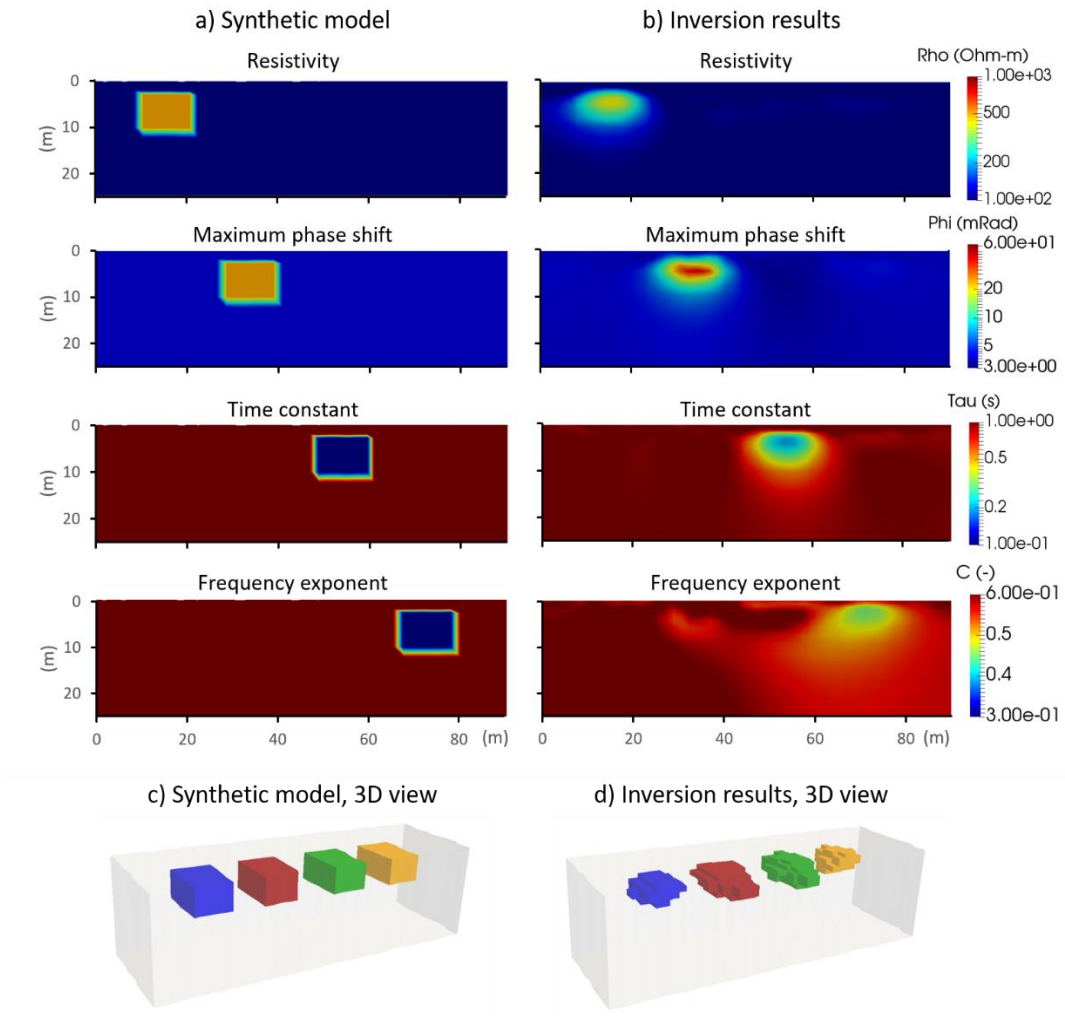

Figure 5: a) Synthetic model with the four MPA Cole-Cole parameters shown as an xz-plane in the middle of the 3D model mesh. b) The inversion results of the synthetic model. c) The synthetic model in a 3D view with the ρ_0 (blue), φ_{max} (red), τ (green), and C (yellow). d) The inversion results in 3D view. The four anomalies are shown for threshold values of $\rho_0 > 200\ Ohmm$ (blue), $\varphi_{max} > 8\ mRad$ (red), $\tau < 0.5\ s$ (green), and $C < 0.5$ (yellow).

8.2 Field example

The measured raw data are signal processed using the scheme described by Olsson *et al.* (2016), where harmonic noise, background drift, and spikes are removed. This automatic signal processing step is followed by a manual processing step, where early time-gates affected by coupling (often seen as fast decaying potentials in the first few time-gates) and outliers are removed. Out of the 1456 quadrupoles, 2% of the resistivity data and 37% of the IP data were removed. Figure 6 (a) shows the number of IP time-gates kept for each quadrupole measurement and Figure 6 (b) shows examples of the measured IP decays and their fit.

The model mesh from the synthetic example is distorted vertically to fit the topography and the forward meshes are generated with topography as well. We apply 1% error bars on the DC data and 10% on the IP data. Furthermore, a factor of 1.5 (2.5 for τ_φ) is used for vertical constraints and 1.2 (1.6 for τ_φ) for lateral constraints between the model parameters of the neighbouring model nodes (same as the synthetic example). The inversion converged after 14 iterations with a data χ-misfit of 1.6 and a total χ-misfit (including constraints) of 1.1. Figure 6 (c) shows the χ-misfit for each of the quadrupole measurements and Figure 6 (d) shows the averaged χ-misfit for the IP data. The timing and memory usage of the inversion are listed in Table 3.

Figure 7 shows the resulting model of the four MPA Cole-Cole parameters in 3D view, while Figure 8 presents a comparison of the inversion results and the borehole information along a 2D slice of the model. Figure 8 (a) shows the geological model of the area, which is constructed based on lithology information from borehole B1 and B2. Figure 8 (b-c) show 2D sections of the 3D inversion results along the northernmost profile (see Figure 4) for the resistivity (ρ_0) and the maximum phase angle (φ_{max}),

respectively. We see that the till and clay/lignite layers identified from the boreholes match well with the high chargeability (Figure 8 c), whereas the low resistivity volume (Figure 8 b) is less continuous and does not match the boreholes as well. The low resistivity anomaly has previously been correlated to a high water conductivity caused by pollution (Maurya *et al.*, 2018). The low water resistivity in the sand is thus shadowing the response from the lithology in the resistivity section. The inversion results, including the τ_φ and C section, agree well with the previous 2D inversion presented in Maurya *et al.* (2016, 2018), who also provide a thorough interpretation of the lithology and the polluted plume.

Four cross-plots of the model parameters retrieved in the model mesh nodes are presented in Figure 9, i.e. the correlation between φ_{max} and the other three parameters as well as the correlation between τ_φ and C. The cross-plots show that no clear correlations are present between the parameters, but that the parameter ranges decrease with depth. This indicates that the variability of the IP parameters in the inversion is data driven, instead of predominantly due to parameter correlations, but that the parameter resolution decreases with depth, as expected.

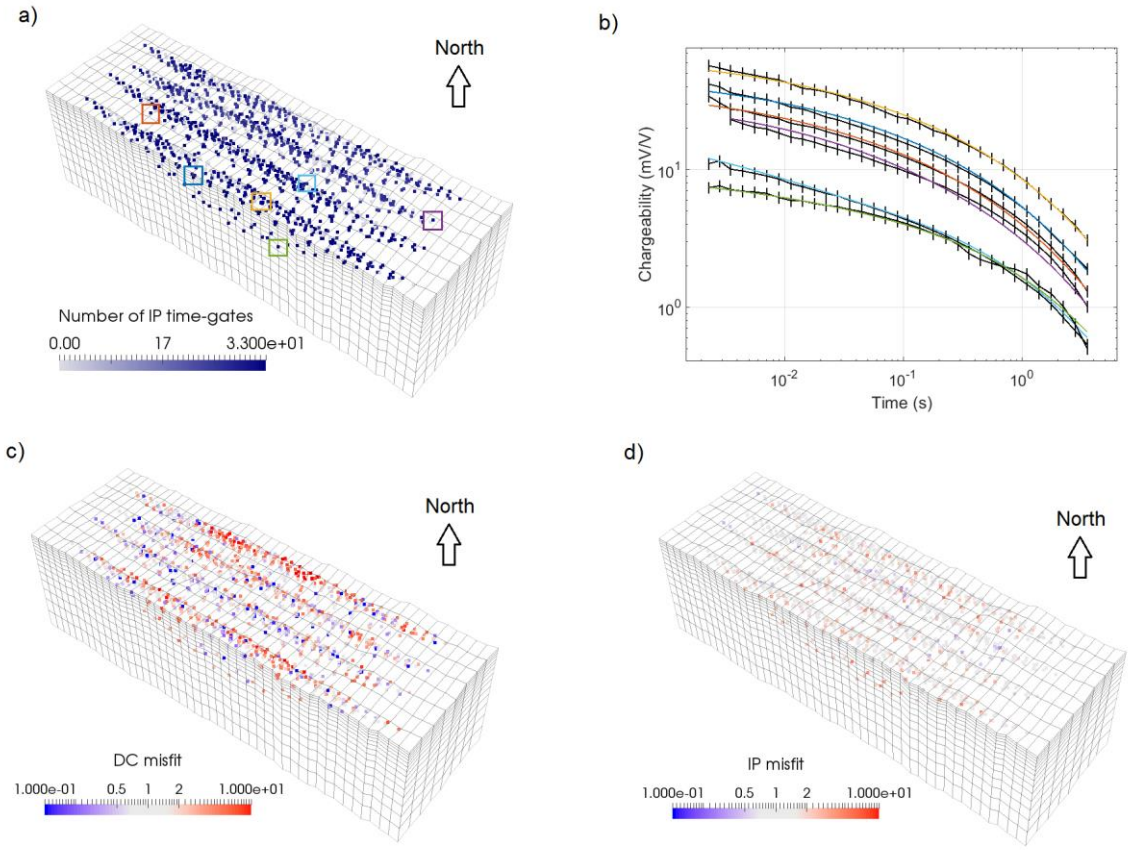

Figure 6: a) Number of IP time-gates kept after processing. b) Measured IP data in black and inversion result shown for selected quadrupole measurements (color-coded to a). c) DC data χ-misfit for each quadrupole measurement shown in a pseudo section. d) IP data χ-misfit for each quadrupole avenged over all time-gates.

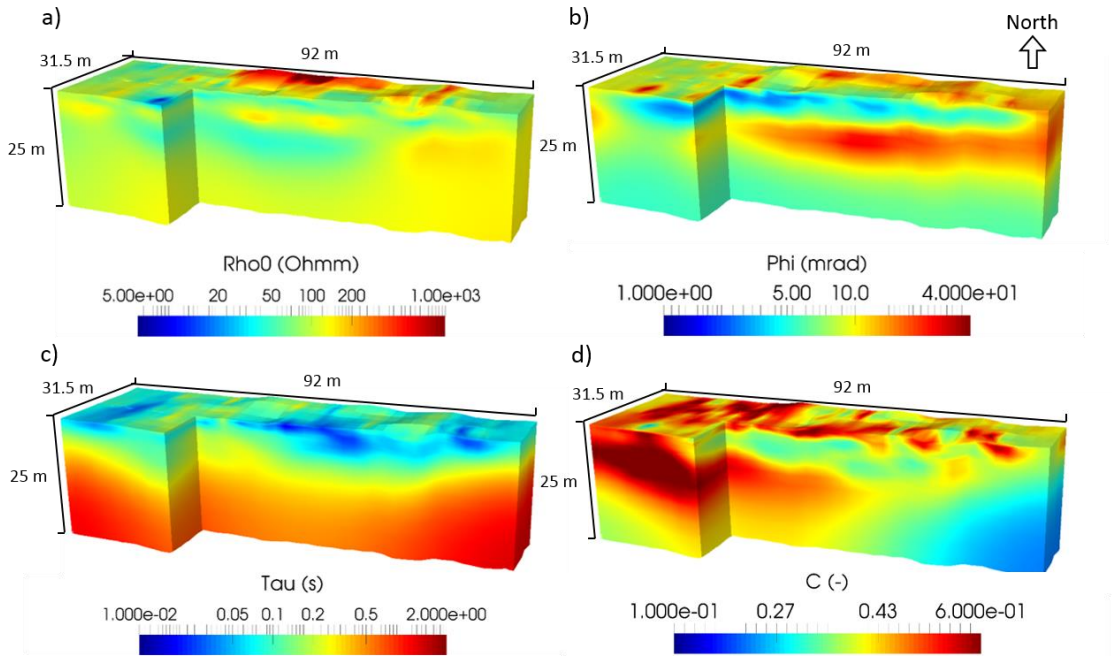

Figure 7: Inversion results of field data from Grindsted Stream (Grindsted, Denmark). The Maximum Phase Angle Cole-Cole model parameters are the resistivity ρ_0 (a), the maximum phase angle φ_{max} (b), the relaxation time τ_φ (c), and the frequency exponent C (d).

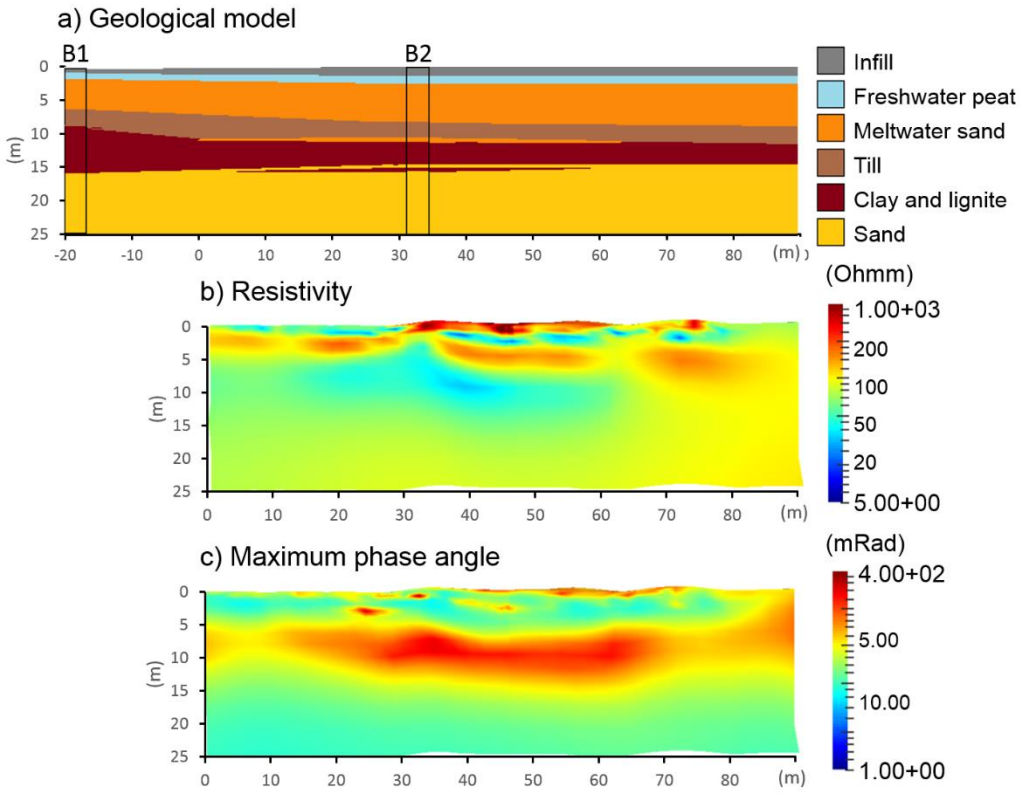

Figure 8: a) Geological model of the area around Grindsted Stream (Grindsted, Denmark) interpreted from lithology description from borehole B1 and B2. b) 2D section of the 3D inversion results along the northernmost profile (see Figure 4) showing the resistivity, ρ_0. c) The same 2D section showing the maximum phase angle, φ_{max}.

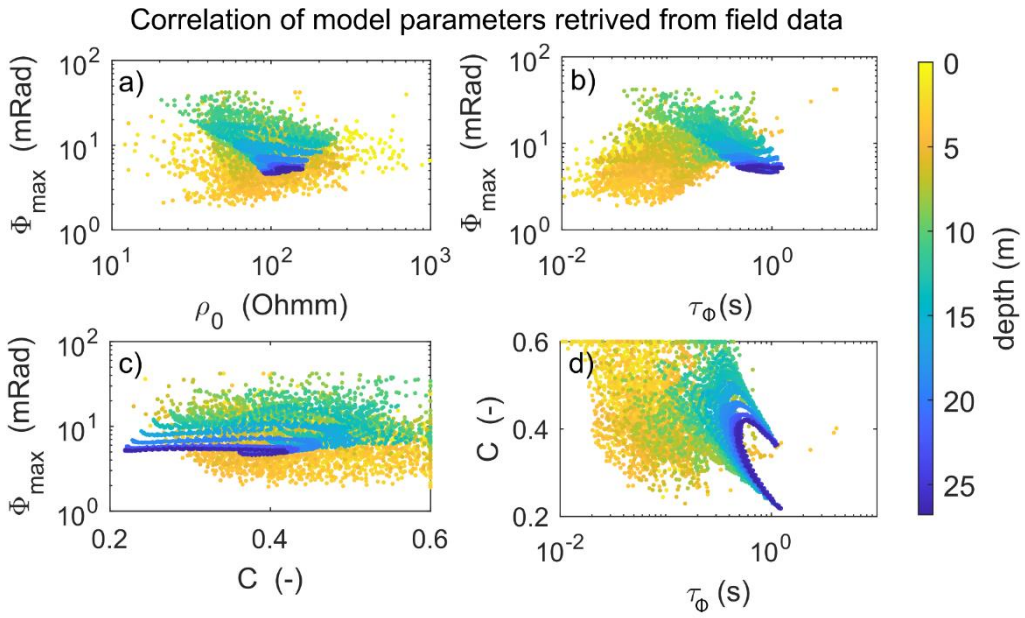

Figure 9: Cross-plot of the model parameter values retrieved from inversion of the field data. The parameters are plotted as maximum phase angle φ_{max} against the three other inversion parameters, i.e. resistivity ρ_0 (panel a), time constant τ_φ (panel b) and frequency exponent C (panel C); furthermore the correlation between τ_φ and C is shown in panel d. The colour indicates the depth of the mesh nodes below the surface.

9. Conclusions

Several codes are available for 1D and 2D spectral inversion of time-domain IP data. These codes solve many problems, but in the case of very complex subsurface structures, 3D modelling is necessary. We have therefore developed a 3D inversion algorithm for resistivity and time-domain spectral IP data, where the forward response is computed in the frequency domain by solving Poisson's equation. The response is then transformed into the time domain, where we take the current waveform into account in order to model, quantitatively, the IP effect and retrieve the full spectral content of the IP signal.

3D spectral inversion of large-scale field datasets is very expensive computationally. In order to keep the inversion time of large-scale field datasets below 24 hours, which is preferable especially in monitoring cases, where data collections are repeated within short time intervals, we have found a significant advantage in applying singularity removal together with an approach for sparsing (down-sampling) the Jacobian matrix. Both methods, which are known from resistivity modelling, have been adapted to the complex IP case, and we have shown that with these adaptions it is possible to carry out spectral 3D inversion of large-scale resistivity and time-domain full-decay IP datasets.

The performance of the proposed inversion algorithm has been demonstrated on a synthetic example with 3D anomalies and a field example with both good data fit and model retrieval. For a dataset with 1256 quadrupoles measurements, each with 33 IP time-gates, an inversion took approximately one hour per iteration using four CPUs. Currently, we are testing the approach for cross-borehole and time-lapse applications with encouraging preliminary results, which we believe will make the algorithm an even stronger tool for field scale environmental applications.

10.Acknowledgement

This work is part of the MIRACHL project (http://mirachl.com/) and is partly founded by Formas – The Swedish Research Council for Environment, Agriculture Science and Spatial Planning (ref. 2016-20099) and partly by the HydroGeophysics Group, Aarhus University (https://hgg.au.dk/).

11.References

Attwa, M., and T. Günther (2013), Spectral induced polarization measurements for predicting the hydraulic conductivity in sandy aquifers, *Hydrol. Earth Syst. Sci*., 17(10), 4079-4094.

Auken, E., Christiansen, A.V., Kirkegaard, C., Fiandaca, G., Schamper, C., Behroozmand, A.A., Binley, A., Nielsen, E., Effersø, F., Christensen, N.B., Sørensen, K.I., Foged, N. & Vignoli, G., 2014. An overview of a highly versatile forward and stable inverse algorithm for airborne, ground-based and borehole electromagnetic and electric data, *Exploration Geophys***,** 46(3), 223-235

Balbarini, N., Rønde, V., Maurya, P., Fiandaca, G., Møller, I., Erik Klint, K., Christiansen, A.V., Binning, P.J. & Bjerg, P.L., 2018. Geophysics Based Contaminant Mass Discharge Quantification Downgradient of a Landfill and a Former Pharmaceutical Factory, *Water Resources Research*, 54(8),5436-5456.

Blaschek, R., Hördt, A. & Kemna, A., 2006. Inversion of SIP data for Cole-Cole and constant-phase-angle relaxation model parameters. *in Near Surface 2006-12th EAGE European Meeting of Environmental and Engineering Geophysics*.

Chapman, B., Gabriele, J. & van der Pas, R., 2007. *Using OpenMP: Portable Shared Memory Parallel Programming*, MIT press.

Christensen, N.K., Ferre, T.P.A., Fiandaca, G. & Christensen, S., 2017. Voxel inversion of airborne electromagnetic data for improved groundwater model construction and prediction accuracy, *Hydrol. Earth. Syst. Sci*, 21, 1321-1337.

Coggon, J.J.G., 1971. Electromagnetic and electrical modeling by the finite element method, *Geophysics*, 36(1)**,** 132-155.

Cole, K.S. & Cole, R.H., 1941. Dispersion and absorption in dielectrics I. Alternating current characteristics, *Journal of Chemical Physics,* 9**,** 341-351.

Dahlin, T. & Zhou, B., 2006. Multiple-gradient array measurements for multi-channel 2D resistivity imaging, *Near Surface Geophysics,* 4**,** 113-123.

Dey, A. & Morrison, H.F., 1979. Resistivity Modeling for Arbitrarily Shaped 2-Dimensional Structures, *Geophysical Prospecting,* 27**,** 106-136.

Fiandaca, G., Auken, E., Gazoty, A. & Christiansen, A.V., 2012. Time-domain induced polarization: Full-decay forward modeling and 1D laterally constrained inversion of Cole-Cole parameters, *Geophysics,* 77**,** E213-E225.

Fiandaca, G., Madsen, L.M. & Maurya, P.K., 2018. Re-parameterisations of the Cole–Cole model for improved spectral inversion of induced polarization data, *Near Surface Geophysics*, 16(4), 385-399.

Fiandaca, G., Olsson, P., Maurya, P.K., Kühl, A., Bording, T.S., Dahlin, T. & Auken, E., 2019. Non-Standard Responses in Time-Domain Induced Polarization Measurements. *in 25th European Meeting of Environmental and Engineering Geophysics, Haag*.

Fiandaca, G., Ramm, J., Binley, A., Gazoty, A., Christiansen, A.V. & Auken, E., 2013. Resolving spectral information from time domain induced polarization data through 2-D inversion, *Geophysical Journal International,* 192**,** 631-646.

Flores Orozco, A., Micić, V., Bücker, M., Gallistl, J., Hofmann, T. & Nguyen, F., 2019. Complex-conductivity monitoring to delineate aquifer pore clogging during nanoparticles injection, *Geophysical Journal International,* 218**,** 1838-1852.

Flores Orozco, A.n., Velimirovic, M., Tosco, T., Kemna, A., Sapion, H., Klaas, N., Sethi, R. & Bastiaens, L., 2015. Monitoring the injection of microscale zerovalent iron particles for groundwater remediation by means of complex electrical conductivity imaging, *Environmental Science & Technology,* 49**,** 5593-5600.

Gazoty, A., Fiandaca, G., Pedersen, J., Auken, E. & Christiansen, A.V., 2012. Mapping of landfills using time-domain spectral induced polarization data: The Eskelund case study, *Near Surface Geophysics,* 10**,** 575-586.

Günther, T. & Martin, T., 2016. Spectral two-dimensional inversion of frequency-domain induced polarization data from a mining slag heap, *Journal of Applied Geophysics,* 135**,** 436-448.

Günther, T., Rücker, C. & Spitzer, K., 2006. Three-dimensional modelling and inversion of dc resistivity data incorporating topography - II. Inversion, *Geophysical Journal International,* 166**,** 506-517.

Hönig, M. & Tezkan, B., 2007. 1D and 2D Cole-Cole-inversion of time-domain induced-polarization data, *Geophysical Prospecting,* 55**,** 117-133.

Hördt, A., Hanstein, T., Hönig, M. & Neubauer, F.M., 2006. Efficient spectral IP-modelling in the time domain, *Journal of Applied Geophysics,* 59**,** 152-161.

Jin, J.-M., 2015. *The finite element method in electromagnetics,* 3rd edition, John Wiley & Sons.

Johansen, H.K. & Sørensen, K.I., 1979. Fast Hankel transforms, *Geophysical Prospecting,* 27**,** 876-901.

Johansson, S., Fiandaca, G. & Dahlin, T., 2015. Influence of non-aqueous phase liquid configuration on induced polarization parameters: Conceptual models applied to a time-domain field case study, *Journal of Applied Geophysics,* 123**,** 295-309.

Karaoulis, M., Revil, A., Tsourlos, P., Werkema, D. D., & Minsley, B. J. (2013). IP4DI: A software for time-lapse 2D/3D DC-resistivity and induced polarization tomography. *Computers & Geosciences, 54*, 164-170.

Kemna, A, 2000. *Tomographic inversion of complex resistivity: theory and application*, thesis, ISBN 3-934366-92-9.

Kemna, A., Binley, A., Cassiani, G., Niederleithinger, E., Revil, A., Slater, L., Williams, K.H., Orozco, A.F., Hegel, F.-H., Hördt, A., Kruschwitz, S., Leroux, V., Titov, K. & Zimmermann, E., 2012. An overview of the spactral induced polarization method for near-surface applications, *Near Surface Geophysics*, 10**,** 453-468.

Lin, C., Fiandaca, G., Auken, E., Couto, M.A. & Christiansen, A.V., 2019. A discussion of 2D induced polarization effects in airborne electromagnetic and inversion with a robust 1D laterally constrained inversion scheme, *Geophysics*, 84**,** E75-E88.

Loke, M.H., Chambers, J.E. & Ogilvy, R.D., 2006. Inversion of 2D spectral induced polarization imaging data, *Geophysical Prospecting*, 54**,** 287-301.

Lowry, T., Allen, M. & Shive, P.N.J.G., 1989. Singularity removal: A refinement of resistivity modeling techniques, 54**,** 766-774.

Madsen, L.M., Fiandaca, G., Auken, E. & Christiansen, A.V., 2017. Time-domain induced polarization - an analysis of Cole-Cole parameter resolution and correlation using Markov Chain Monte Carlo inversion, *Geophysical Journal International*, 211(2), 1341-1353.

Marquart, D.W., 1963. An algorithm lest-squares estimation of non-linear parameters, *J. Soc. ind. appl. Math.*, 11**,** 431-441.

Maurya, P.K., Balbarini, N., Møller, I., Rønde, V., Christiansen, A.V., Bjerg, P.L., Auken, E. & Fiandaca, G., 2018. Subsurface imaging of water electrical conductivity, hydraulic permeability and lithology at contaminated sites by induced polarization, *Geophysical Journal International*, 213**,** 770-785.

Maurya, P.K., Fiandaca, G., Auken, E. & Christiansen, A.V., 2016. Lithological characterization of a comtaminated site using direct current resistivity and time domain induced polarization. *in IP2016/4th International Workshop on Induced Polarization*, Aarhus, Denmark.

Menke, W., 1989. *Geophysical data analysis: discrete inverse theory*, Academic Press, San Diego.

Nivorlis, A., Dahlin, T. & Rossi, M., 2019. Geophysical Monitoring of Initiated In-Situ Bioremediation of Chlorinated Solvent Contamination. *in 25th European Meeting of Environmental and Engineering Geophysics, Haag*.

Nivorlis, A., Tsourlos, P., Vargemezis, G., Tsokas, G., Kim, J. & Yi, M., 2017. Processing and Modeling of Time Domain Induced Polarization Data. *in 23rd European Meeting of Environmental and Engineering Geophysics*.

Oldenburg, D.W. & Li, Y., 1994. Inversion of induced polarization data, *Geophysics,* 59**,** 1327-1341.

Olsson, P.I., Fiandaca, G., Larsen, J.J., Dahlin, T. & Auken, E., 2016. Doubling the spectrum of time-domain induced polarization: removal of non-linear self-potential drift, harmonic noise and spikes, tapered gating, and uncertainty estimation. *in IP2016/4th International Workshop on Induced Polarization*, Aarhus, Denmark.

Pelton, W.H., Ward, S.H., Hallof, P.G., Sill, W.R. & Nelson, P.H., 1978. Mineral discrimination and removal of inductive coupling with multifrequency IP, *Geophysics,* 43**,** 588-609.

Revil, A. & Florsch, N., 2010. Determination of permeability from spectral induced polarization in granular media, *Geophysical Journal International,* 181**,** 1480-1498.

Rücker, C., Günther, T. & Spitzer, K., 2006. Three-dimensional modelling and inversion of dc resistivity data incorporating topography - I. Modelling, *Geophysical Journal International,* 166**,** 495-505.

Schenk, O. & Gärtner, K., 2018. Parallel Sparse Direct And Multi-Recursive Iterative Linear Solvers (PARDISO) - User Guide Version 6.0.0, (https://pardiso-project.org/manual/manual.pdf)

Seigel, H.O., 1959. Mathematical Formulation and type curves for induced polarization, *Geophysics*, 24**,** 547-565.

Shewchuk, J.R., 1996. Triangle: Engineering a 2D quality mesh generator and Delaunay triangulator. *in Workshop on Applied Computational Geometry (*pp. 203-222), Springer, Berlin, Heidelberg.

Si, H.J.A.T.o.M.S., 2015. TetGen, a Delaunay-based quality tetrahedral mesh generator, ACM Transactions on Mathematical Software (TOMS), 41(2), 11.

Spitzer, K., 1998. The three-dimensional DC sensitivity for surface and subsurface sources, *Geophysical Journal International*, 134**,** 736-746.

Van Voorhis, G.D., Nelson, P.H. & Drake, T.L., 1973. Complex resistivity spectra of porphyry copper mineralization, *Geophysics*, 38**,** 49-60.

Weller, A., Slater, L., Binley, A., Nordsiek, S. & Xu, S., 2015. Permeability prediction based on induced polarization: Insights from measurements on sandstone and unconsolidated samples spanning a wide permeability range, *Geophysics*, 80**,** D161-D173.

Wemegah, D., Fiandaca, G., Auken, E., Menyeh, A. & Danuor, S., 2014. Time-domain spectral induced polarization and magnetics for mapping municipal solid waste deposits in Ghana. *in Near Surface Geoscience 2014-20th European Meeting of Environmental and Engineering Geophysics*.

Yi, M., Kim, J. & Son, J., 2012. Simultaneous Inversion of Time-domain SIP Data. *in Near Surface Geoscience 2012–18th European Meeting of Environmental and Engineering Geophysics*.

Yuval & Oldenburg, D.W., 1997. Computation of Cole-Cole parameters from IP data, *Geophysics,* 62**,** 436-448.

Zhao, S. & Yedlin, M.J., 1996. Some refinements on the finite-difference method for 3-d dc resistivity modeling, *Geophysics*, 61(5), 1301–1307.